

Improved Sub-Visible Particle Classification in Flow Imaging Microscopy via Generative AI-Based Image Synthesis

Utku Ozbulak^{1,2*}, Michaela Cohrs³, Hristo L. Svilenov⁴,
Joris Vankerschaver^{1,5}, Wesley De Neve^{1,2}

¹Center for Biosystems and Biotech Data Science, Ghent University
Global Campus, Incheon, Republic of Korea.

²Department of Electronics and Information Systems, Ghent University,
Ghent, Belgium.

³Faculty of Pharmaceutical Sciences, Ghent University, Ghent, Belgium.

⁴Biopharmaceutical Technology, TUM School of Life Sciences,
Technical University of Munich, Freising, Germany.

⁵Department of Mathematics, Computer Science and Statistics, Ghent
University, Ghent, Belgium.

*Corresponding author(s). E-mail(s): utku.ozbulak@ghent.ac.kr;

Abstract

Sub-visible particle analysis using flow imaging microscopy combined with deep learning has proven effective in identifying particle types, enabling the distinction of harmless components such as silicone oil from protein particles. However, the scarcity of available data and severe imbalance between particle types within datasets remain substantial hurdles when applying multi-class classifiers to such problems, often forcing researchers to rely on less effective methods. The aforementioned issue is particularly challenging for particle types that appear unintentionally and in lower numbers, such as silicone oil and air bubbles, as opposed to protein particles, where obtaining large numbers of images through controlled settings is comparatively straightforward. In this work, we develop a state-of-the-art diffusion model to address data imbalance by generating high-fidelity images that can augment training datasets, enabling the effective training of multi-class deep neural networks. We validate this approach by demonstrating that the generated samples closely resemble real particle images in terms

Preprint.

of visual quality and structure. To assess the effectiveness of using diffusion-generated images in training datasets, we conduct large-scale experiments on a validation dataset comprising 500,000 protein particle images and demonstrate that this approach improves classification performance with no negligible downside. Finally, to promote open research and reproducibility, we publicly release both our diffusion models and the trained multi-class deep neural network classifiers, along with a straightforward interface for easy integration into future studies, at github.com/utkuozbulak/svp-generative-ai.

Keywords: Diffusion models, Generative AI, Machine learning, Sub-visible particles

1 Introduction

Sub-visible particles (SvPs) are a critical quality concern in protein-based therapeutics due to their association with a range of adverse effects, including immunogenic responses, reduced drug efficacy, and compromised product stability [1, 2]. The presence of particulate matter can trigger immune activation, potentially leading to anti-drug antibody formation or even anaphylaxis in severe cases [3, 4].

Due to these safety and efficacy concerns, regulatory agencies have issued stringent guidelines to monitor and limit particulate matter in parenteral drugs. The United States Pharmacopeia (USP) and the European Pharmacopoeia mandate the quantification of particles $\geq 10\text{ }\mu\text{m}$ and $\geq 25\text{ }\mu\text{m}$ [5–7]. However, these standards primarily address particle count, often overlooking the chemical nature or morphological characteristics of the particles, which are equally vital for assessing risk and informing root-cause analysis.

Sub-visible particles in biotherapeutics can arise from various sources and are commonly classified into three categories: inherent (consisting of product itself, e.g., protein aggregates), intrinsic (container or delivery system, e.g., glass or rubber), and extrinsic (external contaminants, e.g., fibers or dust) [8]. Certain types of SvPs have been directly linked to reduced therapeutic potency and long-term instability. For example, protein aggregates can cause immunogenic reactions and loss of activity. Meanwhile, other particles, such as particles consisting of silicone oil, which is often used as a lubricant in syringes, are generally considered as low toxic [9, 10]. Nevertheless, even particles that are considered non-toxic can act as catalysts that promote further protein aggregation, indirectly compromising product safety [11]. As a result, accurate detection and classification of SvPs has emerged as a key challenge in pharmaceutical quality control.

To address the challenge of identifying and characterizing SvPs, flow-imaging microscopy (FIM) in combination with machine learning methods – particularly deep learning-based approaches – has emerged as powerful tool [12–15]. These machine learning techniques can learn complex visual patterns, including morphological ones directly from imaging data, enabling automated classification of particle types with greater accuracy compared to traditional rule-based or manual methods [16, 17]. However, one of the main obstacles in applying deep learning to FIM images is the need

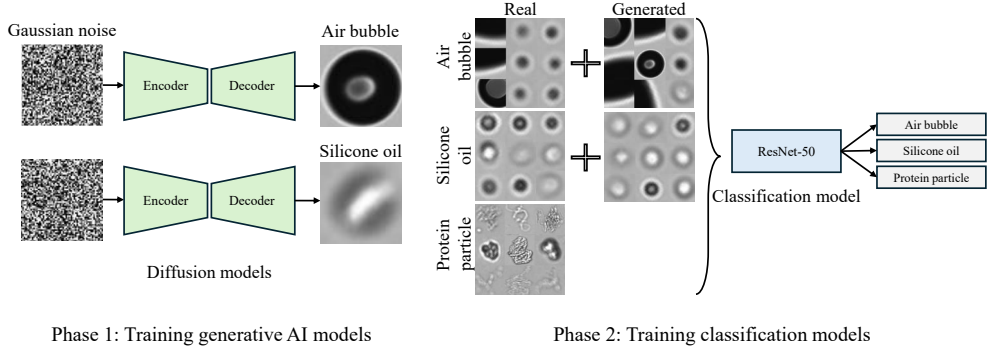


Fig. 1: Visual abstract for the main contribution of the paper. In Phase 1, we train a diffusion-based generative AI model to synthesize SvP images of underrepresented classes (silicone oil and air bubbles). In Phase 2, we train a multi-class classifier using the augmented dataset to demonstrate the usefulness of the generated images in improving classification performance.

for large datasets with balanced numbers of images for the different classes [18]. Deep learning models are notoriously brittle when trained on limited data and are highly sensitive to class imbalance [19]. To address this, some research efforts have explored one-class classifiers, which are more robust under imbalanced conditions, although multi-class classifiers typically offer higher overall classification accuracy [14, 18].

Data scarcity for SvPs is primarily an issue for certain particle types, such as silicone oil droplets and air bubbles, since accurate classification of these particles often requires extensive manual labeling by subject-matter experts [14]. In contrast, acquiring large datasets for protein aggregates is relatively straightforward, as particles can be generated under stress. This creates a unique challenge: despite the availability of abundant data for certain particle types, the overall utility of these datasets is limited in machine learning approaches due to the severe imbalance caused by under-represented particle types. As a result, even large datasets may fail to support robust multi-class learning, highlighting the need for methods that can overcome this hurdle, or generate and augment data for minority classes to ensure balanced and effective model training.

In this work, we address the issue of data imbalance within subvisible particle image datasets by developing a diffusion-based generative model [20] inspired by recent state-of-the-art architectures that have become foundational to many generative image products, including Stability AI’s Stable Diffusion [21], OpenAI’s Sora [22], and Google Gemini [23]. Our focus is on generating high-fidelity images of under-represented particle types, particularly silicone oil droplets and air bubbles, which are challenging to annotate and acquire at scale. By synthetically generating realistic images for these minority classes, our approach enables the full utilization of large SvP datasets without introducing imbalance-related biases, thereby supporting more robust and accurate multi-class classification. An overview of the two-phase approach

is presented in Figure 1: in the first phase, we train a diffusion model to generate high-fidelity synthetic images, and in the second phase, we use these generated images to supplement the training of a multi-class classifier. To further support the community and promote open science, we publicly release our diffusion model, along with sample datasets and implementation code to facilitate its adoption in pharmaceutical quality control and related research applications.

2 Materials and Methods

2.1 Materials

Eight commercial monoclonal antibodies (mAbs) were used to generate protein aggregates. mAbs were formulated in 10 mM acetate buffer, pH 5 at 0.5 mg/ml for heat stress or at 1 mg/ml in 10 mM histidine buffer, pH 6, with 0.9% NaCl and 0.05% polysorbate 20 for mechanical stress. 0.9% NaCl was used to recover silicone oil droplets from siliconized syringes (5 ml Plastipak Luer Lock, BD, Franklin Lakes, US). All solutions were filtered through 0.22 μ m filters before use. All chemicals were pharma grade or higher.

2.2 Sample Preparation and Measurement

Protein aggregates were produced from different mAb solutions via heat or mechanical stress to achieve various morphologies. A digital heat block (VWR, Radnor, USA) was used to heat mAbs in 2 ml microcentrifuge tubes at 90 ° C for 5 or 20 min. Mechanical stress was produced via orbital shaking of 1.35 ml mAb in 2R precleaned glass vials at 300 rpm with 19 mm orbit on a digital orbital shaker (Heathrow Scientific, Illinois, USA) for 48 h.

Silicone oil droplets were recovered from syringes by filling them with 5 ml of 0.9% NaCl and subjecting them to thorough manual agitation for 2 min. 200 μ l of each sample were imaged in triplicates using flow-imaging microscopy (FlowCam 8000, Yokogawa Fluid Imaging Technologies, Scarborough USA). The instrument was equipped with a 10x objective and a 80 x 700 μ m flow cell. A flowrate of 0.15 ml/s in combination with an auto image frame rate of 27 frames/s was used. Particles were captured when 13/10 was exceeded for dark and light pixels. Particles were separated as of 3 μ m distance to nearest neighbor.

Images of air bubbles were manually identified within all samples and separated from the dataset. Those air bubbles were used for machine learning while the remaining dataset was labeled as protein aggregates and silicone oil and also used as described below.

2.3 Dataset Preparation

Using the aforementioned sample preparation protocols, we acquired a total of 520,000 protein particle images as well as 1,500 images of silicone oil and 1,500 images of air bubbles. Due to the resolution variability of the FIM images, we first standardized all images by resizing their smallest edge to 64 pixels. To do that, we followed the

Table 1: Summary of training datasets used for the classification models in this study. Each row represents a different dataset configuration. “Mixed” datasets contain both real and AI-generated images, while “Real” datasets include only real FIM images. All counts are reported in thousands (K), where 1K = 1,000 images.

Dataset Descriptor	Silicone Oil		Air Bubble		Protein Particle	Class Balance
	Real	Generated	Real	Generated	Real	
Real-0	1K	0	1K	0	1K	Balanced
Real-1	1K	0	1K	0	2K	Imbalanced
Real-2					5K	
Real-3					10K	
Real-4					20K	
Mixed-1	1K	1K	1K	1K	2K	Balanced
Mixed-2		4K		4K	5K	
Mixed-3		9K		9K	10K	
Mixed-4		19K		19K	20K	

normalization procedure described in [18]. This ensures a minimum image size of 64×64 while preserving the aspect ratio.

Training Data for Diffusion Models. To prevent data leakage between training and validation, diffusion models are trained exclusively on a separate set of 1,000 real images for each minority class (silicone oil and air bubbles), separate from those used in evaluation. These images served as the basis for learning the generative distribution of underrepresented SvP types.

Validation Data for Classification Models. To provide a consistent and unbiased evaluation baseline, we allocated a fixed validation set comprising 500,000 protein particle images and 500 images each for silicone oil and air bubbles. This heavily imbalanced setup (1000:1 ratio between protein and other classes) reflects real-world class skew and allowed us to robustly assess the predictive performance of models under challenging conditions.

Training Data for Classification Models. From the remaining data (20,000 protein images and 1000 images of silicone oil and air bubbles), as well as the generated data using diffusion models, we constructed multiple training configurations to evaluate the effect of dataset size on classification performance. These configurations fall into two categories below and are summarized in Table 1.

- **Real-n:** Training datasets consisting of only real particle images. The number of samples per class increases progressively across Real-0 to Real-4, ranging from fewer images to a larger number of images with increased data imbalance.
- **Mixed-n:** Training datasets augmented with synthetic images generated via diffusion models. Each Mixed-n set mirrors its Real-n counterpart in real sample count but supplements minority classes (air bubbles and silicone oil) with corresponding generated samples, balancing class distributions while enhancing data diversity.

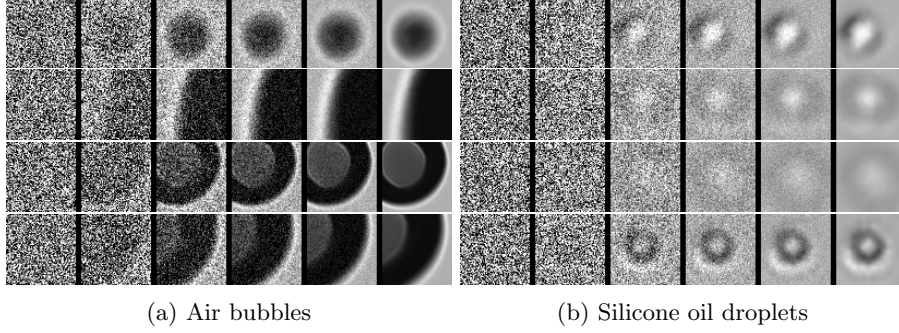


Fig. 2: Visualization of the reverse diffusion process for (a) air bubbles and (b) silicone oil droplets. Each row depicts selected time steps showing the progressive denoising of random noise into structured and realistic sub-visible particle images.

2.4 Diffusion Models

Generative diffusion models are a class of machine learning models designed to generate new data (such as images, sound, or text) by progressively transforming random noise into a structured, meaningful output [20, 24]. These models are based on the concept of diffusion, which refers to the gradual mixing or spreading of particles in a medium [25]. Generative diffusion models consist of two main steps: the forward process (diffusion), where noise is progressively added to the data over time, and the reverse process (denoising), where the model learns to reverse this noise addition, gradually recovering the original data. The forward process transforms the data into pure noise, and the reverse process generates new, meaningful data by denoising the corrupted input, ultimately producing realistic samples.

Forward Process. In the forward process, noise is progressively added to the data (e.g., an image) over several steps, eventually converting it into pure noise. This process, which does not involve a neural network, adds structured noise, such as Gaussian noise. In Denoising Diffusion Probabilistic Models (DDPMs), the type of models we use in this work, the forward process is a Markov chain where noise is added at each step, and the reverse process is learned as a probabilistic model to denoise the data step by step [20].

Let \mathbf{x}_0 represent the original data to which at each step t Gaussian noise is added. The result after t steps, \mathbf{x}_t , is given by:

$$\mathbf{x}_t = \sqrt{\alpha_t}\mathbf{x}_{t-1} + \sqrt{1 - \alpha_t}\epsilon_t$$

In this equation, \mathbf{x}_t is the noisy data at step t , α_t is a hyperparameter controlling the strength of the noise added at each step, typically decaying over time (i.e., $\alpha_t \rightarrow 0$ as t increases), and ϵ_t is Gaussian noise sampled from a normal distribution, $\epsilon_t \sim \mathcal{N}(0, I)$. The forward diffusion process progressively corrupts the data, and as $t \rightarrow T$, the data becomes increasingly noisy, ultimately approaching pure random noise.

Reverse Process. The reverse diffusion process is the core of the generative model. It aims to reverse the noising process by learning the probability distribution $p_\theta(\mathbf{x}_{t-1} | \mathbf{x}_t)$ for each step t , which is given by:

$$p_\theta(\mathbf{x}_{t-1} | \mathbf{x}_t) = \mathcal{N}(\mathbf{x}_{t-1}; \mu_\theta(\mathbf{x}_t, t), \sigma_t^2 I). \quad (1)$$

Here, $\mu_\theta(\mathbf{x}_t, t)$ is the predicted mean of the model for the denoised data at step $t - 1$. The goal is to learn the parameters θ that allow the model to recover clean data from noisy inputs.

Image Generation. The image generation process begins with a sample of pure random Gaussian noise, denoted as \mathbf{x}_T . The goal is to progressively reverse the noising process, step by step, using the learned model to generate a realistic image. As shown in Figure 2, the model applies the learned denoising process starting from the random noise, iteratively refining the noisy image at each step to reconstruct the original data distribution.

At each step t , the model predicts the denoised data \mathbf{x}_{t-1} from the noisy data \mathbf{x}_t by sampling from the learned distribution $p_\theta(\mathbf{x}_{t-1} | \mathbf{x}_t)$, as defined in the reverse process. This process continues until $t = 0$, at which point the generated data \mathbf{x}_0 is a sample from the target distribution, resembling a clean image. The final result is an image that was generated from random noise, having gone through a series of denoising steps, guided by the reverse diffusion process learned during training.

2.5 Model Evaluation

We set up our diffusion model and training environment as described below.

Diffusion Model. Following the work of [20], we used a U-Net architecture with several modifications [26]. First, we replaced standard convolutional layers with weight-standardized convolutional layers, which have been shown to improve training stability and convergence [27]. Second, we incorporated a combination of self-attention and linear attention layers, as these have been demonstrated to enhance the fidelity of generated images [28, 29]. Lastly, we applied Group Normalization before each attention layer [30] to further stabilize training and improve feature normalization.

The forward process described in Section 2.4 consists of multiple noising time steps (T). In our setup, we found that using $T = 1,000$ steps with a linear noise schedule provides the best trade-off between image quality and computational efficiency.

Diffusion Evaluation. To train the diffusion models, we use the L_1 loss between the predicted and ground truth noise at each timestep, which not only encourages sharper reconstructions but also improves the preservation of fine-grained structures in SvP images, which is crucial for distinguishing subtle morphological differences.

The L_1 loss is defined as follows: $\mathcal{L} = \|\hat{\epsilon} - \epsilon\|_1 = \sum_i |\hat{\epsilon}_i - \epsilon_i|$ where $\hat{\epsilon}$ is the predicted noise, ϵ is the ground truth noise, and the summation is over all pixel indices i in the image.

To quantitatively assess the realism of generated images throughout training, we additionally computed the Fréchet Inception Distance (FID). FID compares the distribution of generated images to that of real images in a deep feature space, providing a standard measure of generative quality [31–33]. With the setup described above, we trained our diffusion model for 1,000 epochs on the dataset detailed in Section 2.3. A

		[Predicted class]		
		Silicone oil	Air bubble	Protein
[True class]	Silicone oil	C_{11}	C_{12}	C_{13}
	Air bubble	C_{21}	C_{22}	C_{23}
	Protein	C_{31}	C_{32}	C_{33}

Fig. 3: Confusion matrix illustrating the classification results for three particle types: protein particles, air bubbles, and silicone oil. Each entry C_{ij} represents the number of samples with true class i predicted as class j . Diagonal entries C_{ii} indicate correct classifications, while off-diagonal entries represent misclassifications.

full training cycle for a single model takes approximately 20 hours on a single NVIDIA A6000 GPU.

Classification Model. To evaluate the effectiveness of using diffusion-generated SVP images, we trained two multi-class classification models: a lightweight ResNet-18 and a larger ResNet-50 [34]. These models are trained on the training splits described in Table 1 and evaluated on the validation set detailed in Section 2.3. We applied a grid search strategy using both Adam and AdamW optimizers, exploring ten learning rates $\{10^{-5}, 5 \times 10^{-4}, 10^{-4}, 5 \times 10^{-3}, 10^{-3}, 5 \times 10^{-2}, 10^{-2}\}$ and three weight decay values $\{10^{-5}, 10^{-4}, 10^{-3}\}$, with batch sizes of 32, 64, or 128. This approach results in 126 training outcomes for each model and for each dataset split [35, 36].

Classification Evaluation. To assess classification performance, we report several evaluation metrics computed on an imbalanced validation set, where protein particles vastly outnumber silicone oil and air bubbles.

Given a confusion matrix in the form of Figure 3, let C_{ij} denote the entry of the confusion matrix corresponding to the number of samples whose **true class** is i and **predicted class** is j . Correct classifications appear on the diagonal, i.e., C_{ii} represents the number of particles correctly predicted as class i . Off-diagonal elements C_{ij} for $i \neq j$ correspond to misclassifications from class i to class j .

Given the severe class imbalance, we selected evaluation metrics that are robust to skewed distributions and provide a fair assessment across all classes, including underrepresented ones:

- **Class-based Precision.** Precision (Prec.) is calculated separately for each class to evaluate how many predicted particles of a given type are correctly identified.

$$\text{Precision}_i = \frac{C_{ii}}{\sum_{j=1}^3 C_{ji}} \quad \text{for } i = 1, 2, 3 \quad (2)$$

- **Macro-averaged Class-based Precision.** This metric averages the class-wise precision scores equally across all classes, ensuring that minority classes like air bubbles and silicone oil are not overshadowed by the dominant protein class.

$$\text{Macro-Precision} = \frac{1}{3} \sum_{i=1}^3 \text{Precision}_i \quad (3)$$

- **Precision-Recall Area Under Curve (AUPRC).** This metric evaluates the trade-off between precision and recall across thresholds and is especially informative for rare classes, as it highlights how well the model distinguishes them from the majority class.

$$\text{AUPRC} = \int_0^1 \text{Precision}(r) dr \quad (4)$$

where $\text{Precision}(r)$ is the precision as a function of recall r . The curve is typically constructed by varying the classification threshold and computing precision and recall at each point.

3 Experimental Results

3.1 Diffusion Model Performance

To evaluate the effectiveness of our generative diffusion model in synthesizing realistic SvP images, we first trained separate models for the two most underrepresented particle classes: air bubbles and silicone oil droplets. As described in Section 2.3, each model was trained using only 1,000 real images, carefully excluded from the validation set to avoid data leakage.

In Fig. 4a, we present the training loss for the two diffusion models trained with silicone oil images and air bubble images. Alongside this, Fig. 4b shows the FID scores computed from 100 generated images at various training epochs (1, 5, 10, 20, 50, 100, 200, 500, 1000). As can be seen, although the training loss plateaus around 0.2, the FID continues to improve over time, indicating that the perceptual quality of the generated samples keeps increasing even after the loss converges. This discrepancy suggests that traditional loss values may not fully reflect improvements in sample fidelity, whereas FID provides a more informative measure of generative quality, particularly in capturing subtle visual cues and morphological accuracy relevant to our application. It is important to note, however, that FID values are not inherently meaningful in isolation and should be interpreted relative to the domain: while natural image datasets typically yield lower FID scores, medical and biomedical images – such as our SvP dataset – are expected to produce higher scores [37, 38].

To visualize how this progression manifests in the output quality, we highlight three training epochs in Fig. 4a, from which we sample and present generated images in Fig. 4c and Fig. 4d. As shown in these figures, early-stage outputs (e.g., epoch 5 or 10) are low-fidelity, often exhibiting incomplete particle shapes, indistinct boundaries, and

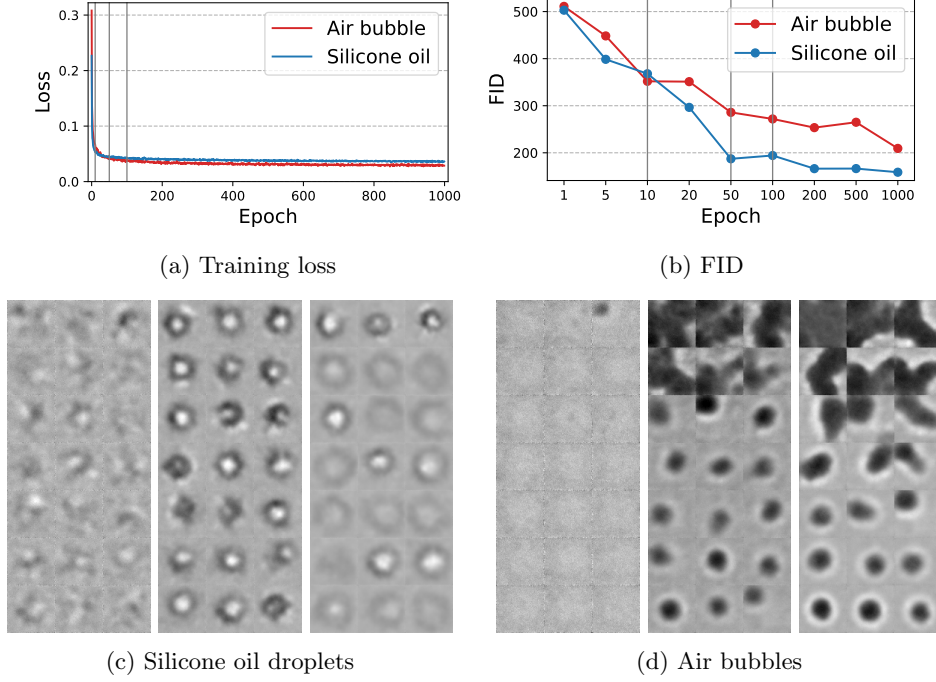


Fig. 4: (a) Training loss curves for the diffusion models. At selected epochs, we generate sample images and compute the Fréchet Inception Distance (FID) between generated and real training images to quantitatively assess generative quality, as displayed in (b). Diffusion-generated images for (c) silicone oil droplets and (d) air bubbles, sampled at epochs 10, 50, and 100, showcasing low-fidelity images that do not resemble real FIM images. The corresponding sampling points are marked in (a) and (b) to contextualize image quality relative to training progression.

missing structural features. In contrast, by epoch 50, the models generate more realistic and coherent particle images, capturing essential characteristics such as spherical morphology, texture, and transparency. This visual progression illustrates how the diffusion models incrementally refine their internal representation of sub-visible particle structure as training advances.

Figure 2 provides a visualization of the denoising process in the reverse diffusion trajectory. Starting from pure Gaussian noise, the model progressively refines the image over 1,000 steps in our setup, gradually introducing particle-specific structures in a visually interpretable manner. To illustrate this process, we present six representative images along the trajectory. This progression highlights the ability of the generative model to recover subtle class-specific features, such as the halo effect in air bubbles or the smooth texture in silicone oil droplets, reinforcing confidence in the utility of these samples for downstream classification.

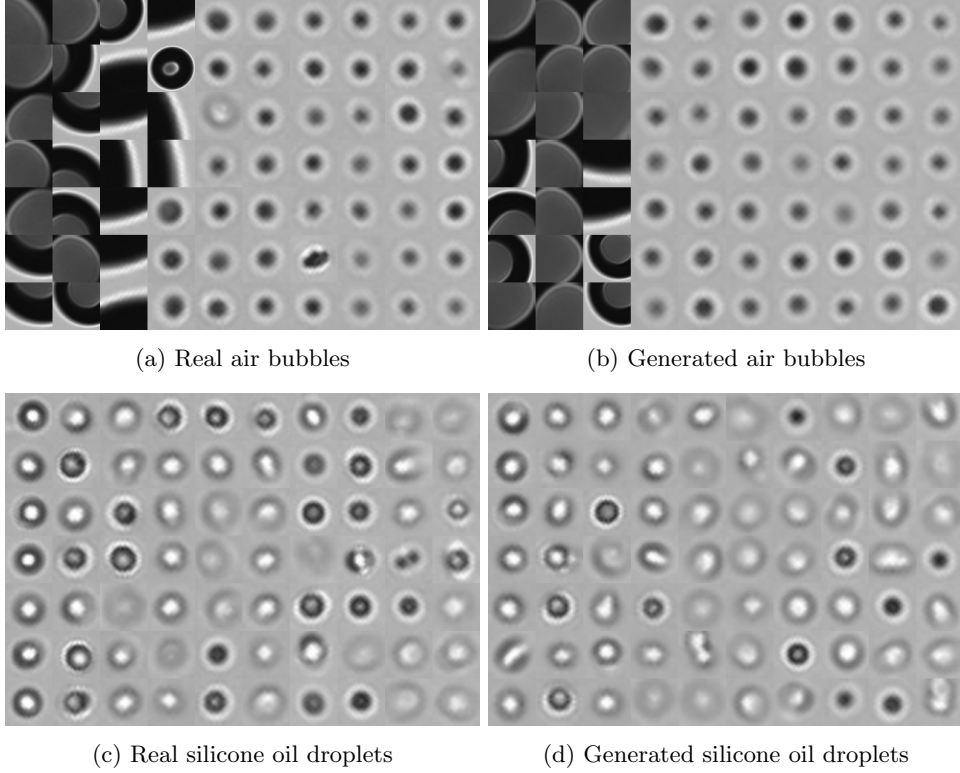


Fig. 5: Examples of diffusion-generated FIM images for underrepresented sub-visible particle types: (b) air bubbles and (d) silicone oil droplets compared to (a-c) real images obtained from FIM. Images on the right are generated by our diffusion models and the ones on the left are FIM images.

The visual quality of the generated samples from the fully trained models is illustrated in Figure 5. As can be seen, the synthesized images closely resemble real FIM images, capturing essential morphological features such as shape irregularities, texture, and transparency. Notably, the generated air bubble images preserve the circular and semi-translucent characteristics typically observed in real samples, while silicone oil droplets exhibit the distinct contour and scattering patterns that differentiate them from other SvP types. These qualitative results suggest that our diffusion models effectively learn the underlying distribution of each particle type, despite the low data regime.

3.2 Classification Model Evaluation

In order to quantify the usefulness of AI-generated SvP images, we conduct a large-scale classification experiment using two deep learning models: ResNet-18 and ResNet-50. As described in Section 2.3, we evaluated the classification performance of models

Table 2: Classification performance on the imbalanced validation set across various training configurations. “Real” datasets contain only the images obtained through FIM, while “Mix” datasets include both FIM and diffusion-generated samples. Results are reported for both ResNet-50 and ResNet-18 models using per-class precision (Prec.), macro-averaged precision, and area under precision-recall curve (AUPRC). For macro-averaged precision and AUPRC, we highlight the best-performing model for the respective dataset split (Real vs Mixed) with bold font.

Model	Training Dataset	Performance on Validation Set				
		Precision				AUPRC
		Silicone Oil	Air Bubble	Protein	Macro	
ResNet-18	Real-0	94.00	98.80	98.06	96.95	89.34
	Real-1	91.60	99.00	99.24	96.61	92.45
	Real-2	92.40	97.60	99.42	96.47	93.01
	Real-3	92.00	99.00	97.86	96.29	90.32
	Real-4	87.80	98.60	99.47	95.29	94.66
	Mixed-1	97.40	98.20	96.83	97.48	92.46
	Mixed-2	95.20	98.60	97.96	97.25	93.09
	Mixed-3	95.00	98.40	98.92	97.44	95.45
	Mixed-4	95.00	99.00	98.61	97.54	96.96
ResNet-50	Real-0	96.35	95.00	97.80	96.38	88.48
	Real-1	99.18	90.00	98.60	95.93	94.85
	Real-2	99.42	89.60	97.00	95.34	95.20
	Real-3	98.22	93.80	98.40	96.81	92.53
	Real-4	98.40	90.80	98.40	96.17	94.77
	Mixed-1	95.60	99.00	96.91	97.17	92.21
	Mixed-2	94.80	99.00	98.32	97.37	95.15
	Mixed-3	96.60	97.40	98.89	97.63	96.93
	Mixed-4	95.20	98.20	99.39	97.60	97.51

on a heavily imbalanced validation set, using multiple training configurations with and without diffusion-generated images. Two architectures, ResNet-18 and ResNet-50, were trained on progressively larger real-only datasets (Real- n) and their augmented counterparts (Mixed- n), allowing us to assess the impact of generated data across different model capacities and data regimes. The results of these experiments, along with evaluation metrics including per-class precision, macro-averaged precision, and AUPRC, are provided in Table 2.

Across both architectures, the addition of diffusion-generated images led to consistent improvements in predictive performance. For instance, in the ResNet-50 experiments, Mixed-3 outperformed its real-only counterpart Real-3 by a margin of 0.82 in macro precision (97.63% vs. 96.81%) and 4.4 points in AUPRC (96.93 vs. 92.53). Similar trends were observed across all Mixed- n variants, with the largest gain observed in Mixed-4, which achieved the highest AUPRC score of 97.51.

For the ResNet-50 architecture, the most notable improvements were observed in the Mixed-3 and Mixed-4 datasets. Compared to their real-only counterparts, these

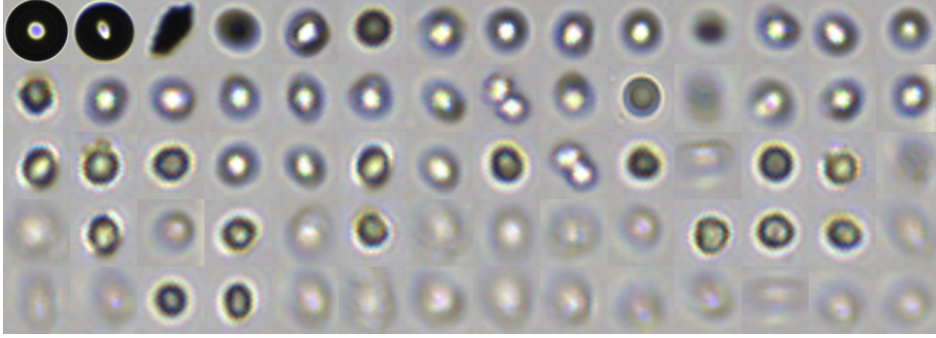


Fig. 6: SvP images labeled as “protein particles” that are consistently misclassified by our classification models.

models achieved macro-averaged precision scores exceeding 97.6%, with AUPRC values reaching up to 97.51. These results indicate that adding synthetic images effectively bridges the gap in predictive performance caused by class imbalance. Interestingly, gains in predictive performance plateaued between Mix-3 and Mixed-4, suggesting that beyond a certain point, additional synthetic data yields diminishing returns.

ResNet-18, despite its shallower architecture, showed similar trends. The best Mixed-n configurations for ResNet-18 achieved macro-precision scores above 97.4 and AUPRC values close to 97.0, closely trailing the deeper ResNet-50 model, suggesting that the benefits of data augmentation extend across different model capacities.

3.3 Misclassified Protein Particles

In Figure 6, we present several SvP images labeled as ‘protein particles’ that are consistently misclassified by our models as silicone oil droplets or air bubbles. Upon initial inspection, many of these particles appear spherical or transparent which are visual traits more commonly associated with silicone oil or air bubbles than protein aggregates. After expert review, we conclude that several of these images are indeed more likely to be silicone oil droplets or air bubbles, indicating possible inaccuracies in the original ground truth labels. In other cases, particularly for the blurry or amorphous particles, the true identity remains uncertain, as such morphology could correspond to protein particles. These observations demonstrate that our model is highly sensitive to subtle morphological differences and, in some cases, may even outperform the original annotations by correctly reclassifying mislabeled examples.

4 Discussion

Our findings demonstrate that diffusion-based generative models provide an effective and scalable solution to the data imbalance problem commonly encountered in SvP classification. By generating high-fidelity synthetic images of underrepresented classes, this approach enables the construction of balanced training datasets without the need for labor-intensive manual annotation. As a result, it becomes possible to fully leverage

the strengths of modern multi-class classifiers, which typically outperform one-class classifiers when sufficient class diversity is present in the training data.

An additional advantage of our method is its adaptability. While this study focused on silicone oil droplets and air bubbles in flow imaging microscopy, the same framework can be applied to other particle types, imaging modalities, or industrial quality control tasks where minority classes are difficult or expensive to annotate. Diffusion models trained on a small set of real samples can effectively synthesize realistic images that capture critical morphological variations, offering a versatile tool for balancing datasets in domains with scarce or sensitive data.

Finally, our work highlights the broader role of generative AI in pharmaceutical manufacturing and quality assurance. By reducing dependence on manual annotation, facilitating reproducible training datasets, and improving classification robustness, diffusion-based generative models have the potential to streamline quality control pipelines and support regulatory compliance in a scalable and data-driven manner. Beyond addressing the immediate challenge of data imbalance in SvP classification, our approach lays the groundwork for the broader adoption of generative AI in biomedical imaging, enabling robust and generalizable machine learning solutions in safety-critical domains.

To promote reproducible research and support future studies, we publicly release our generated datasets, trained diffusion models, and multi-class classifiers at github.com/utkuozbulak/svp-generative-ai.

5 Conclusions

In this study, we developed a generative AI approach using diffusion models to address data imbalance in SvP classification. Using synthesized images of underrepresented particle types, we augmented existing SvP datasets. Our experimental results demonstrate that incorporating these synthetic images into the training data leads to more balanced datasets and improved predictive performance.

Our research highlights the potential of diffusion models to enhance pharmaceutical quality control by reducing reliance on manual annotation and enabling more effective use of machine learning techniques. We anticipate that generative AI will play an increasingly important role in pharmaceutical quality control, offering scalable solutions for data scarcity and enabling more reliable, data-driven decision-making.

Acknowledgments

M.C. is a doctoral fellow from the Research Foundation-Flanders (FWO-V) (grant number 1SH1S24N-7021).

References

- [1] Carpenter, J.F., Randolph, T.W., Jiskoot, W., Crommelin, D.J., Middaugh, C.R., Winter, G., Fan, Y.-X., Kirshner, S., Verthelyi, D., Kozlowski, S., *et al.*: Overlooking subvisible particles in therapeutic protein products: gaps that

- may compromise product quality. *Journal of Pharmaceutical Sciences* **98**(4), 1201–1205 (2009)
- [2] Chisholm, C.F., Soucie, K.R., Song, J.S., Strauch, P., Torres, R.M., Carpenter, J.F., Ragheb, J.A., Randolph, T.W.: Immunogenicity of structurally perturbed hen egg lysozyme adsorbed to silicone oil microdroplets in wild-type and transgenic mouse models. *Journal of Pharmaceutical Sciences* **106**(6), 1519–1527 (2017)
 - [3] Kotarek, J., Stuart, C., De Paoli, S.H., Simak, J., Lin, T.-L., Gao, Y., Ovanesov, M., Liang, Y., Scott, D., Brown, J., *et al.*: Subvisible particle content, formulation, and dose of an erythropoietin peptide mimetic product are associated with severe adverse postmarketing events. *Journal of Pharmaceutical Sciences* **105**(3), 1023–1027 (2016)
 - [4] Uchino, T., Miyazaki, Y., Yamazaki, T., Kagawa, Y.: Immunogenicity of protein aggregates of a monoclonal antibody generated by forced shaking stress with siliconized and nonsiliconized syringes in balb/c mice. *Journal of Pharmacy and Pharmacology* **69**(10), 1341–1351 (2017)
 - [5] United States Pharmacopeial Convention: United States Pharmacopeia <787> subvisible particulate matter in therapeutic protein injections. *Usp-nf general chapter*, United States Pharmacopeia (2021)
 - [6] United States Pharmacopeial Convention: United States Pharmacopeia <788> particulate matter in injections. *Usp-nf general chapter*, United States Pharmacopeia (2025)
 - [7] European Directorate for the Quality of Medicines & HealthCare (EDQM): European Pharmacopoeia 2.9.19: Particulate contamination: sub-visible particles. *European Pharmacopoeia Supplement* 10.3 (2021)
 - [8] Allen Jr, L.V.: Dosage form design and development. *Clinical therapeutics* **30**(11), 2102–2111 (2008)
 - [9] Melo, G.B., Dias Junior, C.d.S., Carvalho, M.R., Cardoso, A.L., Morais, F.B., Figueira, A.C.M., Lima Filho, A.A.S., Emerson, G.G., Maia, M.: Release of silicone oil droplets from syringes. *International Journal of Retina and Vitreous* **5**(1), 1 (2019)
 - [10] Krayukhina, E., Yokoyama, M., Hayashihara, K.K., Maruno, T., Noda, M., Watanabe, H., Uchihashi, T., Uchiyama, S.: An assessment of the ability of submicron-and micron-size silicone oil droplets in dropped prefillable syringes to invoke early-and late-stage immune responses. *Journal of Pharmaceutical Sciences* **108**(7), 2278–2287 (2019)

- [11] Zaman, M., Ahmad, E., Qadeer, A., Rabbani, G., Khan, R.H.: Nanoparticles in relation to peptide and protein aggregation. *International Journal of Nanomedicine*, 899–912 (2014)
- [12] Cohrs, M., Koak, S., Lee, Y., Sung, Y.J., De Neve, W., Svilenov, H.L., Ozbulak, U.: Color flow imaging microscopy improves identification of stress sources of protein aggregates in biopharmaceuticals. In: *International Workshop on Medical Optical Imaging and Virtual Microscopy Image Analysis*, pp. 86–96 (2024). Springer
- [13] Grabarek, A.D., Senel, E., Menzen, T., Hoogendoorn, K.H., Pike-Overzet, K., Hawe, A., Jiskoot, W.: Particulate impurities in cell-based medicinal products traced by flow imaging microscopy combined with deep learning for image analysis. *Cytotherapy* **23**(4), 339–347 (2021)
- [14] Lopez-del Rio, A., Pacios-Michelena, A., Picart-Armada, S., Garidel, P., Nikels, F., Kube, S.: Sub-visible particle classification and label consistency analysis for flow-imaging microscopy via machine learning methods. *Journal of Pharmaceutical Sciences* **113**(4), 880–890 (2024)
- [15] Gambe-Gilbuena, A., Shibano, Y., Krayukhina, E., Torisu, T., Uchiyama, S.: Automatic identification of the stress sources of protein aggregates using flow imaging microscopy images. *Journal of Pharmaceutical Sciences* **109**(1), 614–623 (2020)
- [16] Simonyan, K., Zisserman, A.: Very deep convolutional networks for large-scale image recognition. *International Conference on Learning Representations* (2015)
- [17] Calderon, C.P., Daniels, A.L., Randolph, T.W.: Using deep convolutional neural networks to circumvent morphological feature specification when classifying subvisible protein aggregates from micro-flow images. *arXiv preprint arXiv:1709.00152* (2017)
- [18] Nakae, T., Maruyama, S., Ogawa, T., Hasegawa, S., Obana, M., Fujio, Y.: Application of one-class classification using deep learning technique improves the classification of subvisible particles. *Journal of Pharmaceutical Sciences* **114**(2), 1117–1124 (2025)
- [19] Pecher, B., Srba, I., Bielikova, M.: A survey on stability of learning with limited labelled data and its sensitivity to the effects of randomness. *ACM Computing Surveys* **57**(1), 1–40 (2024)
- [20] Ho, J., Jain, A., Abbeel, P.: Denoising diffusion probabilistic models. *Advances in Neural Information Processing Systems* **33**, 6840–6851 (2020)
- [21] Rombach, R., Blattmann, A., Lorenz, D., Esser, P., Ommer, B.: High-resolution image synthesis with latent diffusion models. In: *Proceedings of the IEEE/CVF*

- Conference on Computer Vision and Pattern Recognition, pp. 10684–10695 (2022)
- [22] OpenAI: Sora: Creating video from text. <https://openai.com/sora/> (2025)
 - [23] Gemini-Team: Gemini: A Family of Highly Capable Multimodal Models. <https://doi.org/10.48550/arXiv.2312.11805>
 - [24] Song, Y., Ermon, S.: Generative modeling by estimating gradients of the data distribution. *Advances in Neural Information Processing Systems* **32** (2019)
 - [25] Sohl-Dickstein, J., Weiss, E., Maheswaranathan, N., Ganguli, S.: Deep unsupervised learning using nonequilibrium thermodynamics. In: *International Conference on Machine Learning*, pp. 2256–2265 (2015). pmlr
 - [26] Ronneberger, O., Fischer, P., Brox, T.: U-net: Convolutional networks for biomedical image segmentation. In: *Medical Image Computing and Computer-assisted intervention–MICCAI 2015: 18th International Conference, Munich, Germany, October 5–9, 2015, Proceedings, Part III 18*, pp. 234–241 (2015). Springer
 - [27] Kolesnikov, A., Beyer, L., Zhai, X., Puigcerver, J., Yung, J., Gelly, S., Houlsby, N.: Big transfer (bit): General visual representation learning. In: *Computer Vision–ECCV 2020: 16th European Conference, Glasgow, UK, August 23–28, 2020, Proceedings, Part V 16*, pp. 491–507 (2020). Springer
 - [28] Vaswani, A., Shazeer, N., Parmar, N., Uszkoreit, J., Jones, L., Gomez, A.N., Kaiser, L., Polosukhin, I.: Attention is all you need. *Advances in Neural Information Processing Systems* **30** (2017)
 - [29] Shen, Z., Zhang, M., Zhao, H., Yi, S., Li, H.: Efficient attention: Attention with linear complexities. In: *Proceedings of the IEEE/CVF Winter Conference on Applications of Computer Vision*, pp. 3531–3539 (2021)
 - [30] Qiao, S., Wang, H., Liu, C., Shen, W., Yuille, A.: Micro-batch training with batch-channel normalization and weight standardization. *arXiv preprint arXiv:1903.10520* (2019)
 - [31] Lucic, M., Kurach, K., Michalski, M., Gelly, S., Bousquet, O.: Are gans created equal? a large-scale study. *Advances in Neural Information Processing Systems* **31** (2018)
 - [32] Heusel, M., Ramsauer, H., Unterthiner, T., Nessler, B., Hochreiter, S.: GANs trained by a two time-scale update rule converge to a local Nash equilibrium. *Advances in Neural Information Processing Systems* **30** (2017)
 - [33] Seitzer, M.: pytorch-fid: FID Score for PyTorch. <https://github.com/mseitzer/pytorch-fid>. Version 0.3.0 (2020)

- [34] He, K., Zhang, X., Ren, S., Sun, J.: Deep residual learning for image recognition. In: Proceedings of the IEEE/CVF Conference on Computer Vision and Pattern Recognition (2016)
- [35] Kingma, D.P., Ba, J.: Adam: A method for stochastic optimization. CoRR **abs/1412.6980** (2014)
- [36] Loshchilov, I., Hutter, F.: Decoupled weight decay regularization. arXiv preprint arXiv:1711.05101 (2017)
- [37] Woodland, M., Castelo, A., Al Taie, M., Albuquerque Marques Silva, J., Eltaher, M., Mohn, F., Shieh, A., Kundu, S., Yung, J.P., Patel, A.B., *et al.*: Feature extraction for generative medical imaging evaluation: New evidence against an evolving trend. In: International Conference on Medical Image Computing and Computer-Assisted Intervention, pp. 87–97 (2024). Springer
- [38] Hashmi, A.U.R., Almakky, I., Qazi, M.A., Sanjeev, S., Papineni, V.R., Jagdish, J., Yaqub, M.: Xreal: Realistic anatomy and pathology-aware x-ray generation via controllable diffusion model. arXiv preprint arXiv:2403.09240 (2024)